Chemical Science

Accepted Manuscript

This article can be cited before page numbers have been issued, to do this please use: J. Dong, Z. Su, Y. Jia, R. Xing, S. She, D. Guan, S. Dai, J. Wang, M. Chai, Z. Hou, Z. Wang, H. Wei, P. Hu and X. Gong, *Chem. Sci.*, 2026, DOI: 10.1039/D5SC09543C.

ROYAL SOCIETY OF CHEMISTRY

rsc.li/chemical-science

View Article Online
DOI: 10.1039/D5SC09543C

ARTICLE

Pd-N-C Shelled Pd Nanoparticle Catalysts for High-Performance Hydrogen Peroxide Electrosynthesis

Received 00th January 20xx,
Accepted 00th January 20xx

DOI: 10.1039/x0xx00000x

Jiao Dong,[‡a] Zixiang Su,[‡bc] Yanyan Jia,[‡d] Runjia Xing,[‡a] Sixuan She,[e] Daqin Guan,[f] Sheng Dai,[d] Jinling Wang,[a] Manqing Chai,[a] Zhenshan Hou,[a] Zhi-Qiang Wang,*[a] Hehe Wei,*[a] P. Hu,[ag] and Xue-Qing Gong*[b]

Metal-nitrogen-carbon (M-N-C) catalysts have attracted very wide attention due to their potential in promoting the electrochemical oxygen reduction reaction (ORR) for the selective production of hydrogen peroxide (H_2O_2). However, the effects of their diverse structures and complex compositions on the catalytic performance remain poorly understood. Herein, systematic theoretical calculations reveal that the Pd-N-C based single-atom catalyst featuring a 1:1 ratio of pyridinic and pyrrolic nitrogen adopts a centrosymmetric PdN_4 structure ($Pd_{SA}N_{2\text{-}2}C$), and the Pd d_{z^2} orbital can strongly interact with the O 2*p* orbital of the adsorbed OOH intermediate, thereby strengthening its adsorption and facilitating subsequent conversion to H_2O_2. Guided by the theoretical insights, the $Pd_{SA}N_{2\text{-}2}C$ catalyst as well as a novel Pd@$Pd_{SA}N_{2\text{-}2}C$ core-shell catalyst with Pd nanoparticles encapsulated by an ultrathin $Pd_{SA}N_{2\text{-}2}C$ shell are synthesized, and the latter exhibits a remarkable H_2O_2 selectivity of 97% and a high yield of 35.88 mol g_{cat}^{-1} h^{-1} at an industrially relevant current density of 200 mA cm^{-2}, along with superior operational stability. This combined theoretical and experimental study provides useful guidance for the rational design of high-efficiency M-N-C catalysts for selective electrocatalysis.

Introduction

Nitrogen-modified-carbon supported metal single-atom catalysts (M-N-C) have shown significant promise for the oxygen reduction reaction (ORR) owing to their structural tunability[1-3], excellent electrical conductivity and low cost[4-8]. The varying types of nitrogen coordination (such as pyridinic, pyrrolic and graphitic nitrogen) as well as the electronic properties of the active metal sites in M-N-C catalysts are expected to be critically important for the two-electron ($2e^-$) ORR toward hydrogen peroxide (H_2O_2) production[9-11]. In particular, significant research efforts have been dedicated to elucidating how the pyridinic- and pyrrolic-nitrogen coordination environments affect the active sites and enhance the catalytic selectivity toward $2e^-$ ORR[12-16]. Through combined theoretical and experimental studies, Chen *et al*. reported that the pyrrole-type CoN_4 single atom catalysts exhibit a remarkable H_2O_2 selectivity of 94% at 0.3 V versus reversible hydrogen electrode (*vs*. RHE) in a flow cell[12], and it was mainly attributed to the increased adsorption strength of OOH, the key intermediate species for H_2O_2 formation, as the result of charge redistribution among the multiple *d* orbitals of the Co after its adsorption. In contrast, Wang *et al*. found that the pyridine-type CoN_4 catalysts exhibit a much lower H_2O_2 selectivity of only 29% at 0.4 V *vs*. RHE. This decrease in selectivity was potentially attributed to the modulation of the metal center by pyridinic N, which leads to a strong H_2O_2 adsorption and subsequent dissociation[13]. Although these studies illustrated that the pyrrole-type M-N-C single-atom catalysts generally exhibit higher $2e^-$ ORR selectivity than the pyridine-type ones, the synergistic effects of different nitrogen coordination environments on the active metal center remain elusive, and the related catalytic mechanisms are also controversial[11-19].

Beyond nitrogen coordination, the selection of the metal center is another crucial determinant of the $2e^-$ ORR selectivity and activity. Several studies have demonstrated that atomically dispersed metal centers coordinated with nitrogen-doped carbon matrices may display divergent catalytic performances in H_2O_2 production. Notably, it has been suggested that the single-atom Pd-N-C catalysts are highly efficient for the $2e^-$ ORR to H_2O_2[18-21]. For example, Jiang *et al*. synthesized a series of single atom catalysts including Pd-N-C, Co-N-C, and Mn-N-C, and they demonstrated that the corresponding H_2O_2 selectivity

[a] State Key Laboratory of Green Chemical Engineering and Industrial Catalysis, Center for Computational Chemistry and Research Institute of Industrial Catalysis, School of Chemistry and Molecular Engineering, East China University of Science and Technology, 130 Meilong Road, Shanghai, 200237, China. E-mail: zhiqiangwang@ecust.edu.cn; weihh@ecust.edu.cn
[b] State Key Laboratory of Synergistic Chem-Bio Synthesis, School of Chemistry and Chemical Engineering, Shanghai Jiao Tong University, 800 Dongchuan Road, Shanghai, 200240, China. E-mail: xqgong@sjtu.edu.cn
[c] National Engineering & Technology Research Center of Scattered Metals, First Rare Materials Co., Limited, Baijia Industrial Park 27-9B, Qingyuan, Guangdong, 511517, China.
[d] Key Laboratory for Advanced Materials and Feringa Nobel Prize Scientist Joint Research Center, School of Chemistry and Molecular Engineering, East China University of Science and Technology, 130 Meilong Road, Shanghai, 200237, China.
[e] Department of Applied Physics, The Hong Kong Polytechnic University, Hung Hom, Kowloon, Hong Kong SAR, China.
[f] WA School of Mines: Minerals, Energy and Chemical Engineering (WASM-MECE), Curtin University, Perth, WA 6102, Australia.
[g] School of Physical Science and Technology, Shanghai Tech University, 393 Middle Huaxia Road, Shanghai, 201210, China.
†Supplementary information (SI) available. See DOI: *xxx*

View Article Online
DOI: 10.1039/D5SC00547C

at 0.82 V *vs*. RHE was 90.3%, 74.8% and 39.8% for these catalysts, respectively[18]. Wang *et al*. confirmed the outstanding performance of the single-atom Pd-N-C catalyst, which achieved approximately 95% H_2O_2 selectivity and an onset potential of ~0.8 V *vs*. RHE[19]. Generally, these findings underscored that both the local nitrogen coordination environment and the identity of the active metal center can tailor the 2e$^-$ ORR performance. Notably, under the alkaline conditions, the 2e$^-$ ORR usually exhibits enhanced activity and selectivity towards the H_2O_2 due to the pH effect[22,23], which can help optimize the intermediate adsorption strength[24] as well as the thermodynamics of ORR processes[25]. Therefore, to unravel the distinct nitrogen coordination motifs and electronic characteristics of catalytic centers at the atomic level is imperative for enabling efficient H_2O_2 electrosynthesis under industrially relevant alkaline conditions.

In this work, by using integrated density functional theory (DFT) calculations and experimental investigations, we elucidated the atomic-level interplay between nitrogen coordination symmetry and *d*-orbital engineering in Pd-N-C catalysts for highly efficient H_2O_2 production via the 2e$^-$ ORR. Our calculated results revealed a synergistic modulation mechanism where a balanced 1:1 ratio of pyridinic to pyrrolic N coordination induces a centrosymmetric PdN_4 structure and promotes the coupling between the Pd d_{z^2} orbital and the 2*p* orbital of the terminal O atom (O_T) of the OOH species binding with the Pd through such O_T. This configuration enhances OOH adsorption and reduces the 2e$^-$ ORR overpotential (η) to 0.54 V, which is significantly lower than that of the previously reported Pd-N-C catalysts (η = 0.77 V)[19]. Guided by the theoretical insights, we employed a dynamic coordination and selective etching (DC-SE) approach for the syntheses of atomically dispersed Pd sites with targeted nitrogen coordination ratios, and an interface-constrained self-assembly (ICSA) strategy for the construction of a novel core-shell type catalyst featuring metallic Pd core encapsulated by the ultrathin (~1.0 nm) N-coordinated Pd shell with a 1:1 coordination of pyridinic and pyrrolic nitrogen (Pd@$Pd_{SA}N_{2\text{-}2}C$). The Pd@$Pd_{SA}N_{2\text{-}2}C$ catalyst delivered exceptional H_2O_2 electrosynthesis performance with a remarkable selectivity of 97%. Moreover, it delivered a high H_2O_2 yield of 35.88 mol g_{cat}^{-1} h^{-1} at an industrially relevant current density of 200 mA cm^{-2} and produced 34.27 g L^{-1} H_2O_2 within 1080 min, demonstrating superior durability and thereby outperforming previously reported catalysts[2,19,26-31]. This work also provides valuable insights into designing high-performance single-atom catalysts through modulating atomic-level coordination symmetry and active-site orbital levels.

Methods

Computational methods

All the structural optimizations and total energy calculations in this work were performed with the spin-polarized DFT by using the Vienna Ab initio Simulation Package (VASP)[32-35]. The Perdew-Burke-Ernzerhof (PBE) functional within the generalized gradient approximation (GGA)[36,37] and the projector augmented wave (PAW) method[38,39] were applied throughout the geometric, electronic and energetic calculations. A cut-off energy of 400 eV was used, and the convergence criteria of energy and force in the calculations were set as 10^{-4} eV/Å and 0.05 eV/Å, respectively.

For the construction of the $Pd_{SA}NC$ model catalyst, we built the *p*(7×7) single-layer graphene structure, where two adjacent C atoms were replaced by one Pd atom and four C atoms around the Pd were further substituted by four N atoms, and one O was also included on the surface to form the C-O-C group. Both pyridinic N and pyrrolic N were considered. To model the core-shell structure of Pd@$Pd_{SA}N_{2\text{-}2}C$, we built the surface slab of Pd(111) covered by a $Pd_{SA}N_{2\text{-}2}C$ layer with minimal lattice mismatch. Specifically, the complex slab contains the $p(9 \times 9)$ $Pd_{SA}N_{2\text{-}2}C$ and $p(8 \times 8)$ Pd(111) which were determined to give a lattice mismatch rate of 0.29%. A vacuum gap of ~10 Å for $Pd_{SA}NC$ surfaces and ~20 Å for Pd@$Pd_{SA}N_{2\text{-}2}C$ surface were used to eliminate the interaction between neighboring slabs. The Brillouin zones were sampled with k-point meshes of $2 \times 2 \times 1$ and $1 \times 1 \times 1$ Gamma grids for $Pd_{SA}NC$ and Pd@$Pd_{SA}N_{2\text{-}2}C$ surfaces, respectively. The calculated ORR mechanisms and other computational details are provided in the Supplementary Information.

Synthesis of Core-Shell Pd@$Pd_{SA}NC$ Catalysts

The Pd@$Pd_{SA}NC$ catalysts were synthesized using an interface-constrained self-assembly strategy[40]. In a typical synthesis, 90 mL of ethanol, 45 mL of ultrapure water, 0.45 mL of ethylenediamine were added to a 250 mL beaker and stirred at the rate of 560 r.p.m. for 30 min. Subsequently, 0.36 g of resorcinol was gently introduced to the above solution and stirred for another 30 min. Concurrently, 0.02 g of $Pd(acac)_2$ was dissolved in 10 mL of ethanol by ultrasonication at 40 ℃. Subsequently, 0.45 mL of formaldehyde and the prepared Pd solution were added into the above beaker and stirred for 24 h at room temperature. The resulting precursors were collected through centrifugation, rinsed three times with ultrapure water and ethanol, and dried at 65 ℃. Next, the dried precursors were placed in an alumina boat and pyrolyzed in a tube furnace under a constant N_2 flow at temperatures of 550 and 950 ℃ for 2 h to synthesize Pd@$Pd_{SA}N_{2\text{-}2}C$ and Pd@$Pd_{SA}N_{3\text{-}1}C$, respectively.

The $Pd_{SA}NC$ materials were synthesized by the dynamic coordination and selective etching process, which involved the co-condensation of Pd precursors (0.02 g $Pd(acac)_2$) with phenolic resin precursors (0.36 g resorcinol and 0.45 mL formaldehyde) and 0.45 mL ethylenediamine, followed by nitrogen-coordination-driven pyrolysis (550 and 950 ℃ for 2 h with N_2 flow) and acid etching (50 mL nitrohydrochloric acid at 50 ℃ for 24 h), which finally generated $Pd_{SA}N_{2\text{-}2}C$ and $Pd_{SA}N_{3\text{-}1}C$, respectively. More details of synthesis are provided in the Supplementary Information.

Electrochemical Measurements

All electrochemical measurements were conducted on a CHI 760E electrochemical workstation at room temperature. The experimental setup comprised a RRDE, an Ag/AgCl reference electrode (saturated by KCl), and a graphite rod as the counter

electrode. The RRDE assembly (IPS Elektroniklabor) consisted of a glass carbon rotating disk electrode (disk area of 0.196 cm^2) and a Pt ring (ring area of 0.159 cm^2). Notably, the experimentally determined apparent collection efficiency under the ferrocyanide/ferricyanide half-reaction system agreed well with the theoretical value of 34.4%. All potentials were calibrated to the RHE according to the equation of $E_{RHE} = E_{Ag/AgCl} + 0.199\ V + 0.059 \times pH - iR \times 85\%$, where pH was measured using a pH meter.

For the preparation of catalytic ink, 4 mg of as-prepared catalyst and 1.5 mg of XC-72R were dispersed in a mixture containing 870 μL of isopropanol, 100 μL ultrapure water and 30 μL Nafion solution (5 wt.%), followed by ultrasonication for 30 min to ensure a homogeneous dispersion. Then, 2.5 μL of ink was drop onto the glassy carbon disk electrode and dried by electrode rotating at 500 r.p.m., yielding a film-coated electrode.

The RRDE measurements were performed in O_2-saturated 0.1 M KOH aqueous solution, over a potential range from 1.1 to 0.1 V *vs*. RHE, at a scan rate of 10 mV s^{-1} and a rotation speed of 1600 r.p.m. During these measurements, the ring electrode was held at a constant potential of 1.2 V *vs*. RHE. Prior to each ORR test, the catalyst was activated by 30 cycles of potential cycling between 1.1 and 0.1 V *vs*. RHE at a scan rate of 50 mV s^{-1} in N_2-saturated 0.1 M KOH solution. Subsequently, the electrolyte was purged with O_2 at least 30 min to ensure optimal ORR conditions. The LSV curves for ORR were obtained by subtracting the currents measured in N_2-saturated 0.1 M KOH, effectively eliminating capacitive currents. The H_2O_2 reduction performance was tested in N_2-saturated 0.1 M KOH containing 10 mM H_2O_2. The stability of the as-prepared catalysts was recorded by the current-time (i-t) chronoamperometric response at 0.1 V *vs*. RHE in an O_2-saturated 0.1 M KOH at 1600 r.p.m. for 60000 s. The H_2O_2 selectivity and the electron transfer number (n) were determined by the following equations:

$$H_2O_2\% = \frac{200I_R/N}{I_D + I_R/N} \quad (1)$$

$$n = \frac{4I_D}{I_D + I_R/N} \quad (2)$$

where I_D is disk current, I_R is ring current, and N is current collection efficiency of the Pt ring.

Results and discussion

Theoretical Exploration of $Pd_{SA}NC$ Catalysts with Specific N Ratios for $2e^-$ ORR

It is well known that the surface structure and composition of the M-N-C catalysts, especially the ratio of pyridinic to pyrrolic N, can significantly influence their ORR activity[11,16,18]. Moreover, as shown in previous studies, the presence of surface O species (particularly in the form of C-O-C groups) may also improve the $2e^-$ ORR activity[3,31,41-43]. Therefore, in this work, we first constructed the Pd-N-C catalyst modified with four pyridinic N atoms and one adsorbed O atom, and progressively replaced the pyridinic N by the pyrrolic one, *i.e.*, $Pd_{SA}N_{4\text{-}0}C$, $Pd_{SA}N_{3\text{-}1}C$, $Pd_{SA}N_{2\text{-}2}C$ and $Pd_{SA}N_{1\text{-}3}C$ (where 4-0, 3-1, 2-2 and 1-3 denote the numbers of pyridinic and pyrrolic N atoms, see Figure 1a-d). For each $Pd_{SA}NC$ catalysts, multiple possible C-O-C configurations at different carbon sites were examined (Figures S1-4 and Tables S1-4), and the thermodynamically most stable structure was selected for all subsequent calculations. Our calculations showed that the $Pd_{SA}N_{4\text{-}0}C$ structure exhibits a high degree of both axial and central symmetries. Then, the introduction of pyrrolic N effectively alters the surface symmetry, resulting in the asymmetric $Pd_{SA}N_{3\text{-}1}C$ and $Pd_{SA}N_{1\text{-}3}C$ structures, while the $Pd_{SA}N_{2\text{-}2}C$ structure is still centrosymmetric around the Pd center. These differences in nitrogen ratios and surface symmetries can modulate the valence state of the single Pd atom. Specifically, the calculated density of states (DOS) (Figure 1e) illustrated that the highest occupied energy levels are from the d_{z^2} orbital in the single-atom Pd of the various $Pd_{SA}NC$ catalysts, while the introduction of pyrrolic N can modify the *d*-orbital configurations of the single Pd atom by causing the disappearance of the $d_{x^2-y^2}$ and the appearance of the d_{xy} at the high energy levels.

To investigate the activity and selectivity of ORR on the $Pd_{SA}N_{4\text{-}0}C$, $Pd_{SA}N_{3\text{-}1}C$, $Pd_{SA}N_{2\text{-}2}C$ and $Pd_{SA}N_{1\text{-}3}C$ catalysts, we systematically calculated the Gibbs free energy changes (ΔG) for the key steps in both $2e^-$ and $4e^-$ ORR processes ($2e^-$ associative pathway: $O_2 + 2(H_2O + e^-) \rightarrow H_2O_2 + 2OH^-$, $4e^-$ associative pathway: $O_2 + 4(H_2O + e^-) \rightarrow 2H_2O + 4OH^-$) on these catalysts (Figures S5-10). The computational details are presented in *Supplementary Methods: ORR mechanism and calculation details*. It is widely accepted that the catalytic selectivity towards H_2O_2 formation over H_2O is critically governed by the thermodynamics of the key intermediates, and a key descriptor for predicting this selectivity is the Gibbs free energy of *O (ΔG(*O))[44,45]. This is because that, to make H_2O_2 production thermodynamically favorable, the O-O bond scission for the surface *OOH intermediate must be suppressed, and this can be achieved when the ΔG(*O) is higher than 3.52 eV ($\Delta G_{H_2O_2}$-ΔG_{H_2O})[44-47]. Our results showed that the calculated ΔG(*O) values for the $Pd_{SA}NC$ catalysts are all higher than 3.52 eV (the corresponding ΔG(*O) values are 3.63, 4.24, 4.81 and 4.92 eV for $Pd_{SA}N_{4\text{-}0}C$, $Pd_{SA}N_{3\text{-}1}C$, $Pd_{SA}N_{2\text{-}2}C$ and $Pd_{SA}N_{1\text{-}3}C$, see Figure S1), indicating a high selectivity for H_2O_2 production on these catalysts. At the same time, it can be noticed that the steps with the maximum ΔG (ΔG_{max}) during the $2e^-$ ORR are identical at various $Pd_{SA}NC$ catalysts, *i.e.*, the potential determining step (PDS) is the first step: $O_2 + H_2O + e^- + * \rightarrow *OOH + OH^-$. The corresponding overpotentials (η) were calculated to be 1.25 V, 0.63 V, 0.54 V and 0.59 V for the $Pd_{SA}N_{4\text{-}0}C$, $Pd_{SA}N_{3\text{-}1}C$, $Pd_{SA}N_{2\text{-}2}C$ and $Pd_{SA}N_{1\text{-}3}C$ catalysts, respectively, clearly showing that $Pd_{SA}N_{2\text{-}2}C$ gives the highest $2e^-$ ORR activity (Figure 1f).

To understand the differences in $2e^-$ ORR activity and selectivity among these $Pd_{SA}NC$ catalysts, we performed DOS and Bader charge analyses to investigate the adsorption of key intermediates during the reaction processes on these catalyst surfaces. The calculated results revealed that on all the $Pd_{SA}NC$ catalysts, the *OOH intermediate binds to the Pd sites (with the O atom directly bonding with Pd being defined as O_T). Although a weak hydrogen-bond interaction between the H atom in *OOH and the O atom in C-O-C group can help stabilize *OOH, this effect is common to all $Pd_{SA}NC$ catalysts, and the C-O-C group does not alter the Bader charge of the Pd center (Figures 1a-d, S11 and 12). The stability of the resulting Pd-O_T bond mainly originates from electron transfer from the d_{z^2} orbital of Pd to the O_T 2*p* orbital (see Figures 1e, 1g and S10, Tables S5

and 6). The amount of electron transferred in this process follows the order: $Pd_{SA}N_{2\text{-}2}C$ > $Pd_{SA}N_{1\text{-}3}C$ > $Pd_{SA}N_{3\text{-}1}C$ ≈ $Pd_{SA}N_{4\text{-}0}C$ (with transferred charges being calculated to be 0.225, 0.159, 0.103 and 0.108 |e|, respectively, see Table S5). In addition, we also found that on the surfaces where both pyridinic- and pyrrolic-N exist, in comparison with the $Pd_{SA}N_{4\text{-}0}C$ surface, the energy level of the d_{xy} orbital is lowered upon OOH adsorption, which may further indicate the enhancement of OOH adsorption.

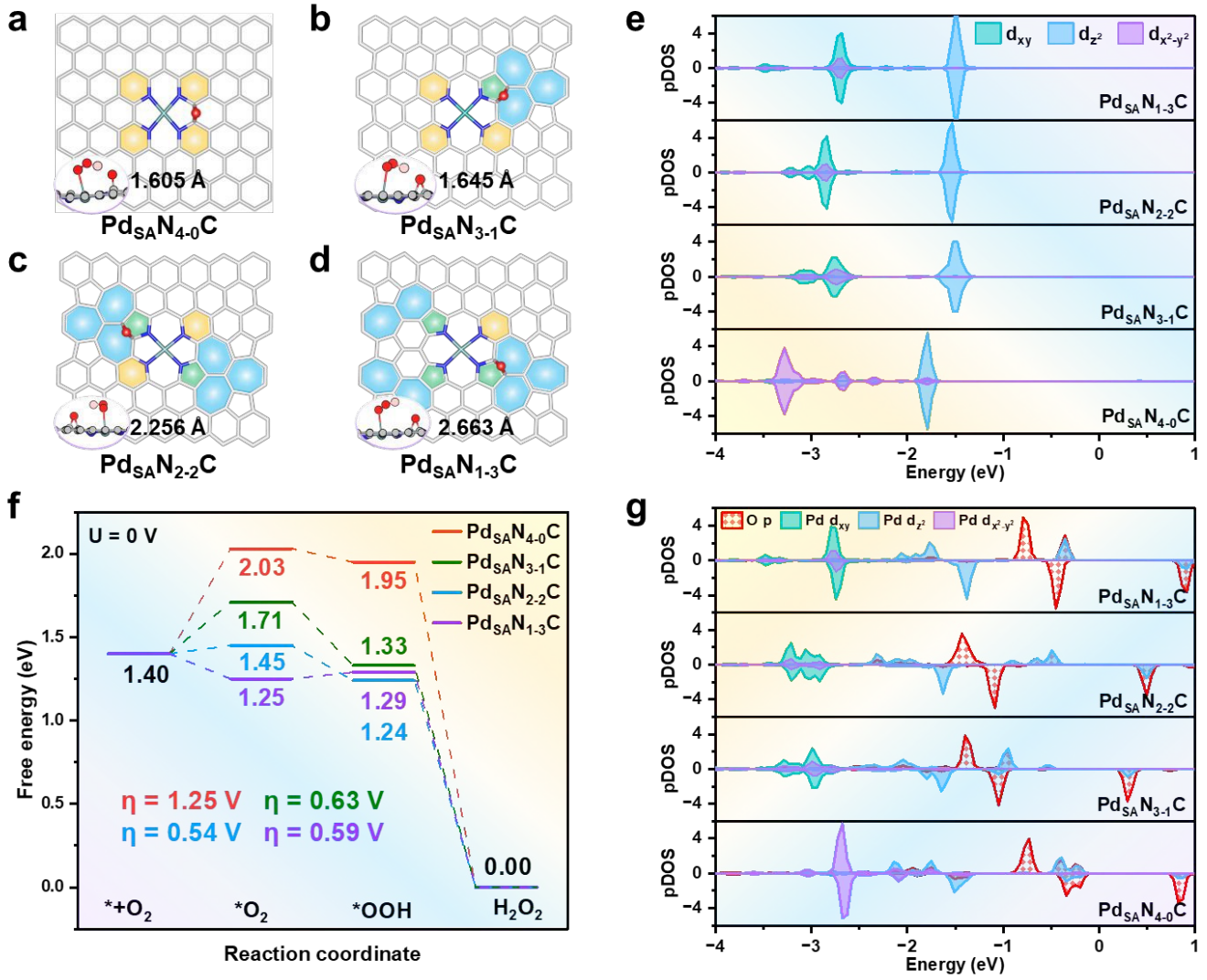

Fig. 1 DFT calculations of the ORR processes and electronic properties of various $Pd_{SA}NC$ catalysts. Calculated structures (top view) of (a) $Pd_{SA}N_{4\text{-}0}C$, (b) $Pd_{SA}N_{3\text{-}1}C$, (c) $Pd_{SA}N_{2\text{-}2}C$ and (d) $Pd_{SA}N_{1\text{-}3}C$ catalysts and those with OOH adsorption (insert: side view). Green: Pd, blue: N, red: O, grey: C, pale pink: H. Hydrogen bonds are shown in the diagram. (e) Calculated partial density of states (pDOSs) of the split *d* orbitals of Pd single-atom at various $Pd_{SA}NC$ catalysts. (f) Calculated free energy profiles of 2e⁻ ORR pathway and the corresponding overpotentials of different catalysts. (g) Calculated pDOSs of the *p* orbitals of O_T in *OOH and split *d* orbitals of Pd single-atom of $Pd_{SA}NC$ catalysts. All DOSs were aligned with respect to the 2*s* orbital of one specific C atom in the complete hexagonal ring of the catalysts.

Furthermore, we observed that as the content of pyrrolic N increases, the calculated Bader charge on the single atom Pd becomes more positive (0.709, 0.702, 0.712, and 0.741 |e| for $Pd_{SA}N_{4\text{-}0}C$, $Pd_{SA}N_{3\text{-}1}C$, $Pd_{SA}N_{2\text{-}2}C$ and $Pd_{SA}N_{1\text{-}3}C$, respectively, see Figure S13). It clearly showed that a moderate (neither too high nor too low) positive Bader charge on the Pd site is favorable for OOH adsorption. Nevertheless, the $Pd_{SA}N_{2\text{-}2}C$ surface still exhibits the largest Bader charge change for the Pd after OOH adsorption, reaching 0.119 |e| (Figure S13). Finally, we further calculated the electrostatic interaction energies (E_{inter}) between the O_T atom of the adsorbed OOH species and the Pd active site, which again confirms that the $Pd_{SA}N_{2\text{-}2}C$ surface interacts most strongly with the *OOH species (E_{inter} values for $Pd_{SA}N_{4\text{-}0}C$, $Pd_{SA}N_{3\text{-}1}C$, $Pd_{SA}N_{2\text{-}2}C$ and $Pd_{SA}N_{1\text{-}3}C$ are -1.27 eV, -1.28 eV, -1.50 eV and -1.35 eV, respectively, see Table S7), in excellent agreement with the calculated 2e⁻ ORR activity of the $Pd_{SA}NC$ catalysts.

Interestingly, our results can reveal a direct linear correlation between electron transfer and electrostatic interaction across the different $Pd_{SA}NC$ configurations: systems exhibiting larger electron transfer consistently display stronger electrostatic

View Article Online
DOI: 10.1039/D5SC09543C

interactions (Figure S14). Specifically, different N-coordination environments modulate the energy levels distribution of Pd *d*-orbitals; the resulting changes further tune the ability of Pd to transfer electrons to *OOH, thereby strengthening the electrostatic interaction between Pd and the terminal O atom (O_T) in *OOH and ultimately governing the adsorption strength of *OOH. From the above discussion, we can conclude that the centrosymmetric $Pd_{SA}N_{2\text{-}2}C$ surface, with its balanced pyridinic-to-pyrrolic N ratio, can regulate the *d*-orbital distribution of the Pd center to transfer more electrons and achieve stronger electrostatic stabilization, and help it maintain a moderate Bader charge, thereby facilitating OOH adsorption and leading to excellent 2e$^-$ ORR catalytic activity.

Syntheses and Characterizations of Novel Pd-N-C Catalysts

Inspired by the theoretical predictions of the optimal nitrogen coordination ratio for the electrochemical synthesis of hydrogen peroxide via the 2e$^-$ ORR, we tentatively synthesized two prototypical single-atom $Pd_{SA}NC$ catalysts, $Pd_{SA}N_{2\text{-}2}C$ (with high activity) and $Pd_{SA}N_{3\text{-}1}C$ (with low activity), both featuring the coexistence of pyridinic and pyrrolic nitrogen species. To rationally engineer these $Pd_{SA}NC$ catalysts, we developed two distinct synthetic strategies. Firstly, a dynamic coordination and selective etching approach[40] was used to construct these single-atom $Pd_{SA}NC$ catalysts with atomically dispersed Pd-N sites and tunable pyridinic-to-pyrrolic N distributions. Transmission electron microscopy (TEM) and high-angle annular dark-field scanning transmission electron microscopy (HAADF-STEM) images confirmed the atomic dispersion of Pd in the as-prepared $Pd_{SA}NC$ catalysts (Figures S15-17). X-ray photoelectron spectroscopy (XPS) analysis revealed that the $Pd_{SA}N_{2\text{-}2}C$ and $Pd_{SA}N_{3\text{-}1}C$ catalysts synthesized in this way indeed possess optimized pyridinic-to-pyrrolic nitrogen ratios of 1:1 and 3:1, respectively (Figure S18). Notably, the $Pd_{SA}N_{2\text{-}2}C$ catalyst exhibited approximately 64% higher ring current (i_{ring}) and 16% higher disk current density (j_{disk}) than $Pd_{SA}N_{3\text{-}1}C$, with these performance enhancements being consistently observed across a broad potential window ranging from 0.3 to 0.6 V *vs*. RHE. Furthermore, the $Pd_{SA}N_{2\text{-}2}C$ exhibited exceptional electrocatalytic performance, with a hydrogen peroxide selectivity close to 93% and a transferred electron number (n) of 2.2, which is also a significant improvement over $Pd_{SA}N_{3\text{-}1}C$ (77% selectivity, n = 2.5) as evidenced by the rotating ring-disk electrode (RRDE) measurement (Figures S19-22). The general consistency between experimental results and theoretical calculations suggested that the nitrogen coordination engineering strategy for the construction of a centrosymmetric structure can potentially give rise to the enhanced 2e$^-$ ORR activity and selectivity.

Secondly, an interface-constrained self-assembly strategy (Figure 2a) was used to form a N-containing resin precursor on Pd, followed by pyrolysis under N_2 to generate a structure in which Pd nanoparticles are encapsulated by an ultrathin Pd-N-C shell. By varying the pyrolysis temperature, the pyridinic/pyrrolic N distribution in the shell can be tuned. Specifically, at relatively lower temperatures, pyrrolic-N in pentagonal ring structures is more readily retained within the forming carbon matrix. As the temperature increases, additional dehydrogenation and structural rearrangement favor the formation of thermodynamically more stable pyridinic-N sites in hexagonal rings, leading to a corresponding increase in the proportion of pyridinic-N. Intriguingly, the as-prepared catalyst gave the conformation with a $Pd_{SA}NC$ shell encapsulating the Pd nanoparticle, *i.e.*, a Pd@$Pd_{SA}NC$ core-shell architecture was obtained through this synthesis strategy (Figure 2b-e). The TEM measurement revealed that the core-shell Pd@$Pd_{SA}NC$ catalysts exhibit a nanosphere morphology, showing Pd nanocrystals with an average size of 21.9 nm (Figures 2b and S23-25) encapsulated by a $Pd_{SA}NC$ shell with the thickness of 1.0 nm (Figure 2c-e). The core-shell structure was further confirmed by HAADF-STEM images (Figures S26 and 27). Moreover, the uniform distribution of Pd, N, O, and C atoms in the shell of Pd@$Pd_{SA}NC$ was evidenced by STEM energy dispersive X-ray spectroscopy (EDS) mapping (Figures S28 and 29). Overall, these findings suggested that following an interface-constrained self-assembly strategy, the structural evolution of the catalyst is mainly originated from the suppression of Pd aggregation mediated by oxygen-containing functional groups. This modulation also facilitates lattice match between metallic Pd and graphitic carbon domains during pyrolysis, thus promoting the epitaxial growth of nitrogen-doped carbon shells.

Then, the electronic properties of the Pd@$Pd_{SA}NC$ catalysts were analyzed using XPS (Figures 2f and S30-35) and X-ray absorption spectroscopy (XAS). The deconvoluted C 1*s* XPS spectra revealed peaks at 284.8 eV (sp^2-hybridized C-C), 285.9 eV (C-O/C-N), 287.3 eV (C=O), 288.9 eV (COOH), and 290.7 eV (π-π^*) (Figure S33a). The peak positions for both Pd@$Pd_{SA}N_{2\text{-}2}C$ and Pd@$Pd_{SA}N_{3\text{-}1}C$ remained virtually unchanged, with their corresponding peak area ratios also showing no significant variation. Combined with the Raman spectra (Figure S33b), the I_D/I_G values of Pd@$Pd_{SA}N_{2\text{-}2}C$ and Pd@$Pd_{SA}N_{3\text{-}1}C$ are both less than 1, indicating that the carbon defect contents of both are relatively low[48-50]. Therefore, we can expect that the main source of its 2e$^-$ ORR activity is not the carbon framework itself. The high-resolution N 1*s* XPS spectra of Pd@$Pd_{SA}N_{2\text{-}2}C$ (Figure 2f) shows three prominent subpeaks at 398.4, 399.6 and 400.9 eV, corresponding to the pyridinic-, pyrrolic- and graphitic-N, respectively. The combined atomic content of pyridinic- and pyrrolic-N in Pd@$Pd_{SA}N_{2\text{-}2}C$ was determined to be 4.17 at%, with their atomic ratio approximating 0.8 (close to 1:1, see Figure S35 and Table S8). In contrast, the Pd@$Pd_{SA}N_{3\text{-}1}C$ exhibited a ratio of 3:1 for these two nitrogen species. Hence, although the two Pd@$Pd_{SA}NC$ catalysts demonstrated similar carbon shell with similar carbon species and carbon defects, accompanied by atomically dispersed Pd, the Pd@$Pd_{SA}N_{2\text{-}2}C$ and Pd@$Pd_{SA}N_{3\text{-}1}C$ catalysts featured distinctive functional moieties in carbon shell, including the pyridinic- and pyrrolic-N, with a ratio close to 1:1 and 3:1, respectively. Complementary XAS results provided critical information of the Pd chemical states. In the X-ray absorption near-edge structure (XANES) analysis, the absorption edges of these Pd@$Pd_{SA}NC$ catalysts shift to higher

View Article Online
DOI: 10.1039/D5SC09547C

energy compared with the metallic Pd foil, indicating partially oxidized Pd (Figure S36). Extended X-ray absorption fine structure (EXAFS) analysis further reveals a pronounced metal peak at ~2.5 Å, corresponding to Pd-Pd coordination (Figure 2g), together with an additional feature at ~1.5 Å that can be assigned to the Pd-N coordination[1-3] (Figures S37 and 38). It should be noted that because the bond lengths of Pd-N and Pd-O are nearly identical, structural assignment based solely EXAFS fitting carries uncertainly. To further support the presence of Pd-N coordination, the color change observed during catalyst preparation and the UV-Vis results (Figures S39 and S40) were provided. These results indicated that, at the early stage of the liquid-phase synthesis, ethylenediamine effectively replaces the original acetylacetonate ligands and preferentially pre-coordinates with the Pd centers, thereby providing the basis for the formation of Pd-N coordination in the final catalyst. The fitted Pd-N coordination number is 3.89 (Table S9), suggesting the presence of Pd-N bonds within the PdN_4 structures. The integration of the morphological characterizations and XPS analysis of Pd 3*d* gave compelling evidence for the existence of core-shell structure, where the oxidized Pd species with nitrogen coordination constitute the $Pd_{SA}NC$ shell, while the metallic Pd form the encapsulated Pd nanoparticle core[51].

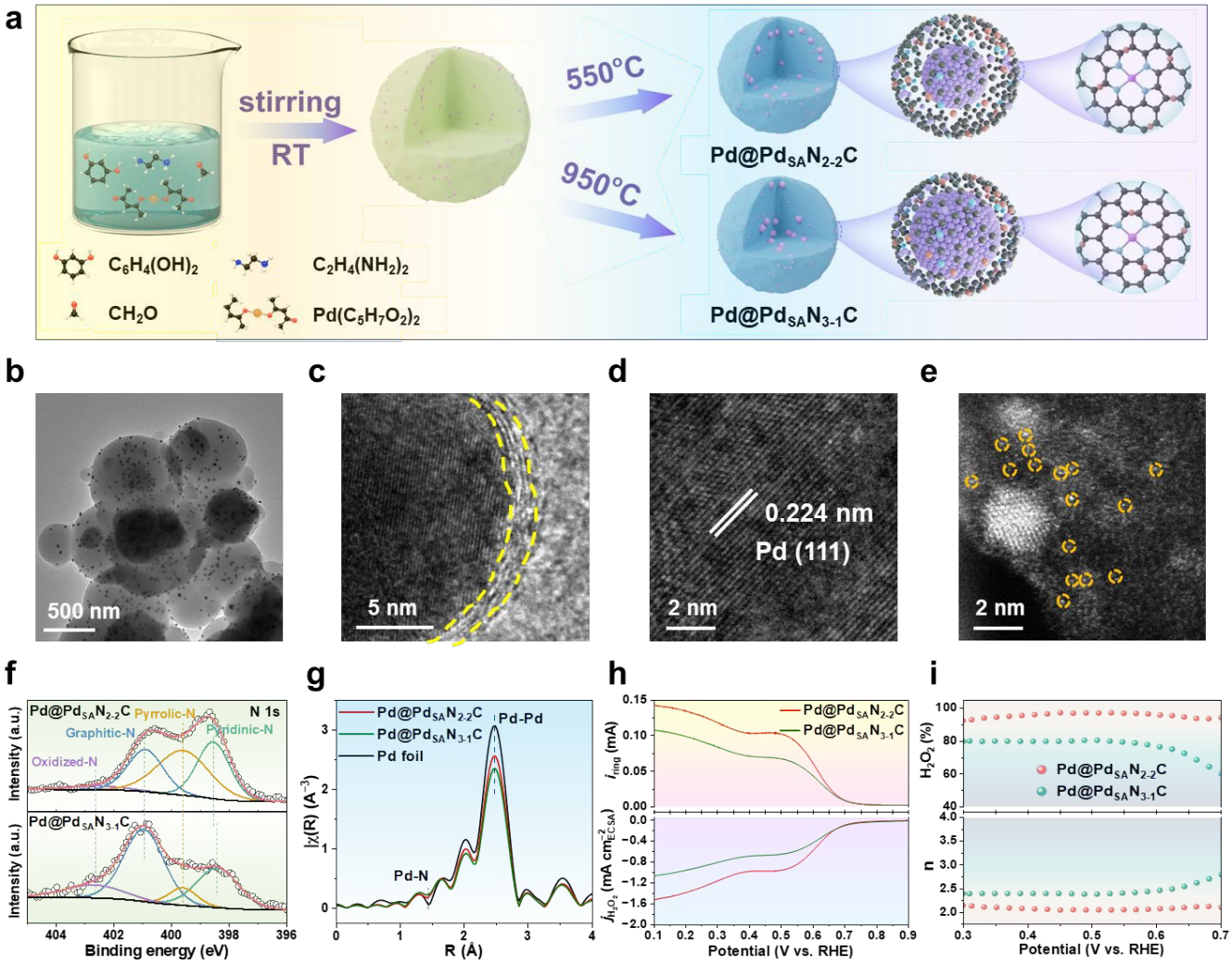

Fig. 2 Synthesis and characterization of Pd@$Pd_{SA}NC$ catalysts. (a) Schematic illustration of the interface-constrained self-assembly strategy for the syntheses of Pd@$Pd_{SA}NC$. (b) TEM, (c, d) HRTEM and (e) STEM images of the Pd@$Pd_{SA}N_{2\text{-}2}C$ catalyst. (f) XPS spectra of N 1*s* and (g) EXAFS spectra of Pd@$Pd_{SA}NC$ catalysts. (h) Linear sweep voltammetry (LSV) curves of the ring current density and current density of H_2O_2 generation normalized by ECSA, (i) H_2O_2 selectivity and electron transfer number of ORR toward H_2O_2.

Intriguingly, the H_2O_2 selectivity of Pd@$Pd_{SA}N_{2\text{-}2}C$ was the highest among those of the various $Pd_{SA}NC$ and Pd@$Pd_{SA}N_{3\text{-}1}C$ catalysts, accompanied by the significantly enhanced intrinsic activity (Figures 2h and S20, 41-46), indicating its superior ORR performance. Specifically, the Pd@$Pd_{SA}N_{2\text{-}2}C$ catalyst achieved approximately 97% hydrogen peroxide selectivity and a transferred electrons number of 2.1 across a very broad potential range from 0.3 to 0.7 V *vs*. RHE, outperforming those of the previously reported catalysts[2,19,26-31] (Figures 2i, S47 and 48, Table S10). Furthermore, RRDE measurement revealed that the Pd@$Pd_{SA}N_{2\text{-}2}C$ catalyst also exhibited accelerated electron transfer kinetics and exceptional mass activity (Figures S49 and 50). However, RRDE tests are often affected by O_2 diffusion. In practical applications using a flow-cell measurement, which

View Article Online
DOI: 10.1039/D5SC09547C

effectively overcomes the influence of mass transfer, it can be anticipated that Pd@$Pd_{SA}N_{2-2}C$ would achieve more efficient H_2O_2 synthesis.

Theoretical Evidence for the High Performance of Pd@Pd_{SA}NC in 2e$^-$ ORR

To elucidate the reason for the enhanced 2e$^-$ ORR activity of the Pd@Pd_{SA}NC catalysts, we modeled and calculated the characteristic Pd@$Pd_{SA}N_{2-2}C$ structure with the minimal lattice mismatch rate of 0.29% (Table S11). It was constructed with the metallic Pd slab as the core covered by the Pd_{SA}NC single layer containing pyridinic and pyrrolic N at a 1:1 ratio (Figure 3a). We then systematically calculated the Gibbs free energy changes for the key steps of the 2e$^-$ and 4e$^-$ ORR processes on this Pd@$Pd_{SA}N_{2-2}C$ catalyst (Figures 3b and 3c, S51 and 52). The results showed that the ΔG(*O) on the Pd@$Pd_{SA}N_{2-2}C$ is 4.36 eV (Figure S52), which is greater than the benchmark of 3.52 eV[44-47], indicating a preference for the 2e$^-$ ORR pathway and the H_2O_2 production. We also found that the calculated η of such core-shell Pd@$Pd_{SA}N_{2-2}C$ catalyst (η = 0.04 V) is much lower than that of the $Pd_{SA}N_{2-2}C$ catalyst (η = 0.54 V) and the Pd-N-C materials reported in the literature as well (η = 0.77 V)[19], which aligns well with our experimental results.

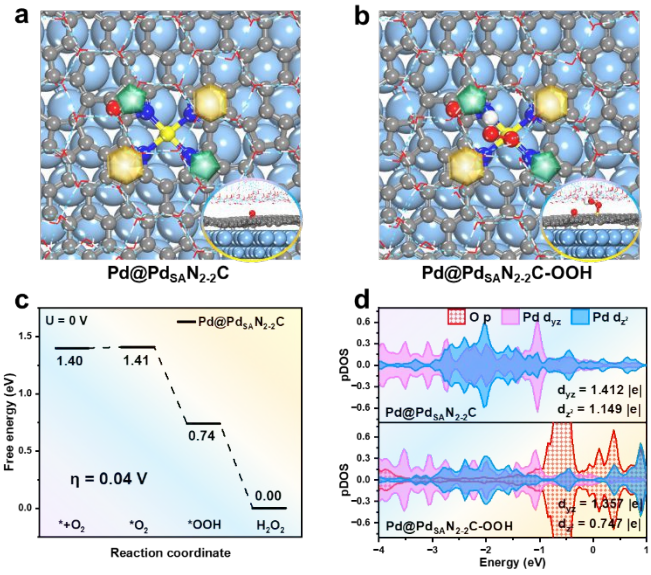

Fig. 3 Theoretical calculations of ORR toward H_2O_2 formation at Pd@$Pd_{SA}N_{2-2}C$ catalyst. (a) Calculated surface and (b) OOH adsorption structures of Pd@$Pd_{SA}N_{2-2}C$ catalyst (top view; insert: side view). Yellow: Pd single-atom, blue: N, red: O, white: H, grey: C, light blue: bulk Pd atoms, red and white lines: H_2O molecules. (c) Calculated free energy profile of 2e$^-$ ORR on the Pd@$Pd_{SA}N_{2-2}C$ surface. (d) Calculated pDOSs of the *p* orbital of O_T in *OOH and *d* orbitals of Pd single-atom in Pd@ Pd_{SA}NC catalyst shells.

To further understand the fundamental reasons behind the high activity and selectivity of the Pd@$Pd_{SA}N_{2-2}C$ catalyst in the 2e$^-$ ORR process, we first carried out DOS calculations for the key intermediates on the surface. The results demonstrated that during the formation of the bond between the *OOH species and the single-atom Pd on the Pd@$Pd_{SA}N_{2-2}C$ surface, the electron occupation of the Pd d_{z^2} orbital is significantly reduced by 0.402 |e| (Figure 3d), which is nearly twice of that determined for the $Pd_{SA}N_{2-2}C$ catalyst (0.225 |e|, Table S5). Furthermore, Bader charge analysis revealed that, although the single atom Pd sites in both $Pd_{SA}N_{2-2}C$ and Pd@$Pd_{SA}N_{2-2}C$ catalysts possess similar Bader charges (0.712 and 0.718 |e|, respectively), the change in Bader charge of the shell Pd single atoms after OOH adsorption is more pronounced for the latter (0.119 and 0.125 |e| for $Pd_{SA}N_{2-2}C$ and Pd@$Pd_{SA}N_{2-2}C$, respectively, Figure S53). Notably, further calculations revealed that the core Pd cluster also promotes the electrostatic interaction between the single-atom Pd site in the $Pd_{SA}N_{2-2}C$ shell and the O_T in *OOH (the corresponding electrostatic interaction energy is -2.43 eV, see Figure S53). To further investigate the role of the metallic Pd core, we calculated the *d*-band center of Pd on the $Pd_{SA}N_{2-2}C$ and Pd@$Pd_{SA}N_{2-2}C$ surfaces, as well as that of the shell ($Pd_{SA}N_{2-2}C$(Pd@$Pd_{SA}N_{2-2}C$)) and the core (Pd(Pd@$Pd_{SA}N_{2-2}C$)) in Pd@$Pd_{SA}N_{2-2}C$. The results indicate that the single-atom Pd in the $Pd_{SA}N_{2-2}C$(Pd@$Pd_{SA}N_{2-2}C$) shell has the lowest *d*-band center (Table S12), suggesting that the metallic Pd core can modulate the *d*-band center of the surface single-atom Pd via charge transfer, thereby optimizing the OOH adsorption and enhancing the 2e$^-$ ORR performance of Pd@$Pd_{SA}N_{2-2}C$.

Structure-Activity Relationship of the Pd@$Pd_{SA}N_{2-2}C$ Catalyst

Detailed experimental tests were conducted to better illuminate the catalytic activity of the Pd@$Pd_{SA}N_{2-2}C$ catalyst. In-situ attenuated total reflection Fourier-transform infrared spectra (ATR-FTIR) were obtained for the ORR process at various potentials ranging from 0.9 to 0.0 V *vs*. RHE, and they revealed three distinct peaks, where the peak at 1236 cm^{-1} corresponds to the O-O stretching of the adsorbed OOH, while the peaks at about 1397 cm^{-1} and 1457 cm^{-1} may originate from the adsorbed H_2O_2 and O_2, respectively (Figure 4a). Most importantly, the intensity of the broad *OOH peak increased as the applied potential decreased from 0.9 to 0.0 V *vs*. RHE (Figure 4b), confirming that the 2e$^-$ ORR pathway indeed occurs on the Pd@$Pd_{SA}N_{2-2}C$ surface.

In addition, to elucidate the effect of the Pd single atom within the Pd_{SA}NC shell on the ORR activity and selectivity, a comparative study was performed by utilizing the commercial Pd/C and the Pd_{SA}NC catalysts. The results showed that the exposed Pd nanoparticles in commercial Pd/C mainly facilitate the 4e$^-$ ORR pathway (Figure S54), while the abundant surface Pd single atom in the Pd_{SA}NC shell of the Pd@$Pd_{SA}N_{2-2}C$ catalyst serve as key active sites to promote the ORR process for H_2O_2 production. This conclusion was further confirmed by the SCN$^-$ poisoning experiment. Upon the addition of 10 mM KSCN, the disk current density decreased immediately by 9.6% (Figure S55), further indicating that the Pd species are the main catalytic sites. This is in line with the electronic properties illustrated by the theoretical calculations discussed earlier.

Furthermore, the long-term stability of the Pd@$Pd_{SA}N_{2-2}C$ catalyst was evaluated using the chronoamperometry assessments at a constant potential of 0.1 V *vs*. RHE. Over 60000 s of continuous 2e$^-$ ORR operation, both the disk and ring currents remained largely unchanged, and the H_2O_2 selectivity

View Article Online DOI: 10.1039/D5SC09543G

remained above 97% without any obvious decrease (Figure 4c). The very small current density of the H_2O_2 reduction reaction (H_2O_2RR) observed in Pd@$Pd_{SA}N_{2-2}C$ (Figure 4d) indicated its negligible activity for H_2O_2RR.

To rigorously assess the electrocatalytic performance of the Pd@$Pd_{SA}N_{2-2}C$ catalyst for H_2O_2 synthesis under actual operating conditions, we conducted tests using an advanced three-phase flow cell setup (Figures S56 and 57). The results further demonstrated that Pd@$Pd_{SA}N_{2-2}C$ exhibited a high catalytic activity, with the H_2O_2 yield exceeding 15 mol g_{cat}^{-1} h^{-1} at the current densities from 100 to 200 mA cm^{-2}. Specifically, the H_2O_2 yield of Pd@$Pd_{SA}N_{2-2}C$ reached 35.88 mol g_{cat}^{-1} h^{-1} at 200 mA cm^{-2}, with a H_2O_2 Faradic efficiency (FE) of 86.55% and mass activity of 870 A_{H2O2} g_{cat}^{-1}. Compared with those of most reported electrocatalysts, this result demonstrates the relatively superior performance of our material, particularly in terms of H_2O_2 yield (Figures 4e and S58, Table S13). Notably, even in 1.0 M KOH, Pd@$Pd_{SA}N_{2-2}C$ demonstrated a superior H_2O_2 formation activity of 50 mol g_{cat}^{-1} h^{-1} and a H_2O_2 FE of approximately 90% (Figure S59). These results suggested that the core-shell Pd@$Pd_{SA}N_{2-2}C$ catalyst with a 1:1 ratio of pyridinic to pyrrolic N indeed exhibits a remarkable H_2O_2 generation rate at industrially relevant current densities.

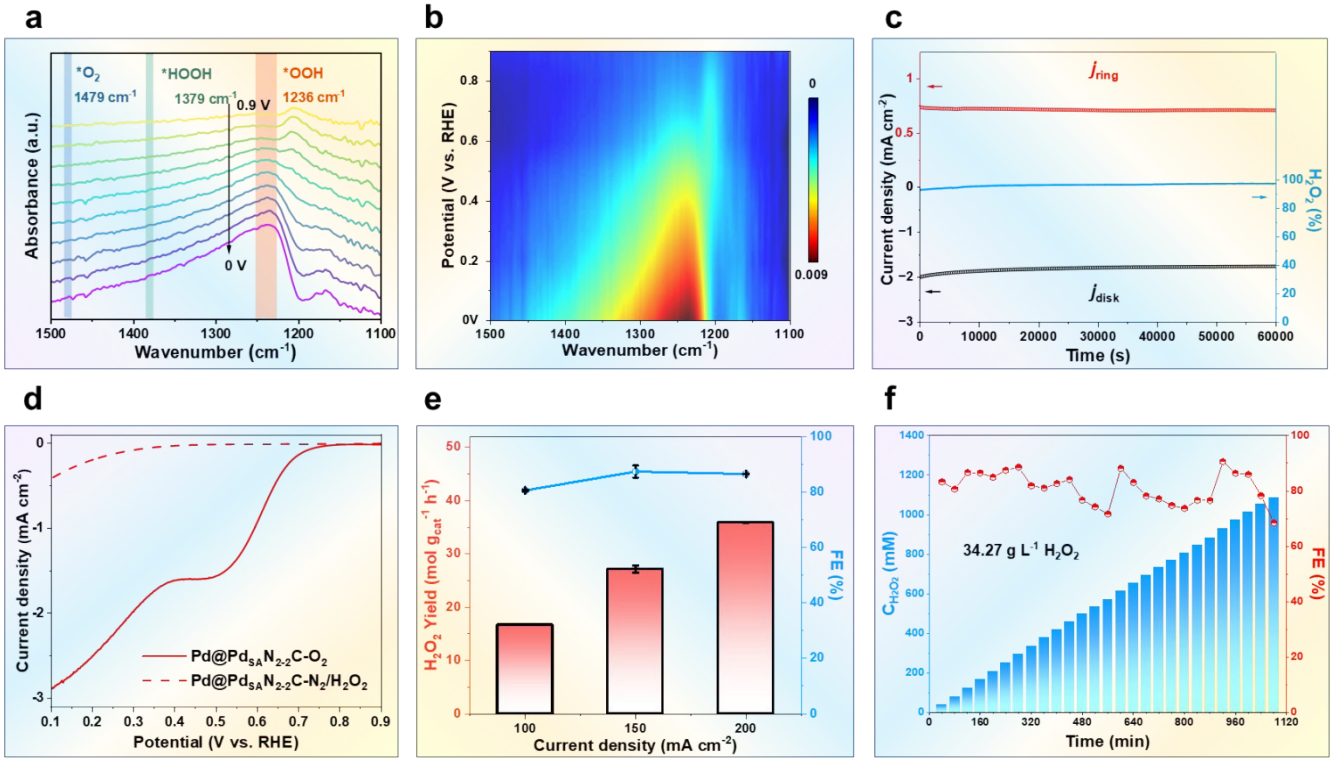

Fig. 4 Electrocatalytic 2e⁻ ORR performances and mechanisms for Pd@$Pd_{SA}N_{2-2}C$ catalyst. (a, b) *In-situ* ATR-SEIRAS spectra at different potentials from 0.9 to 0.0 V *vs.* RHE. (c) Stability at 0.3 V *vs.* RHE. (d) LSV curves of H_2O_2RR and ORR. (e) H_2O_2 yields and Faradic efficiency (FE) at the current densities from 100 to 200 mA cm^{-2}. (f) Continuous tests for H_2O_2 production for 1080 min at 200 mA cm^{-2}.

Moreover, the large-scale continuous productivity and electrochemical stability of Pd@$Pd_{SA}N_{2-2}C$ were further evaluated in 0.1 M KOH at 200 mA cm^{-2}. During the test, the potential remained stable at around -0.1 V *vs*. RHE (Figure S60), and the H_2O_2 FE remained higher than 80%. Continuous electrolysis at 200 mA cm^{-2} for 1080 min gave a sustained high H_2O_2 yield, achieving a concentration of up to 34.27 g L^{-1} (Figure 4f). Post-test XRD patterns, TEM images and XPS spectra of the catalyst showed neglectable changes (Figures S61-64). These findings demonstrated that the Pd@$Pd_{SA}N_{2-2}C$ catalyst can maintain excellent H_2O_2 generation performance even under scaled-up operation conditions, highlighting its superior efficacy and versatility.

Conclusions

In summary, we have systematically investigated the effects of local structures and nitrogen environment in Pd-N-C catalysts on the electrochemical 2e⁻ ORR for H_2O_2 formation through the combined theoretical and experimental studies. The DFT calculated results revealed that the $Pd_{SA}N_{2-2}C$ catalyst, featuring a 1:1 ratio of pyridinic to pyrrolic N atoms, exhibited superior activity for the 2e⁻ ORR. This exceptional activity was attributed to the centrosymmetric structure of PdN_4 and the involvement of the d_{z^2} orbital of the single Pd atom in the formation of stable Pd-O bonds with the 2*p* orbital of O_T species in the adsorbed OOH intermediate. Furthermore, experimental efforts enabled the successful synthesis of both the $Pd_{SA}N_{2-2}C$ catalyst and a complex one with core-shell nanostructure, where the exposed two-dimensional structure involving atomically dispersed Pd atoms with tailored nitrogen coordination serves as the shell and the Pd nanoparticle as the core. The Pd@$Pd_{SA}N_{2-2}C$ catalyst

exhibited an excellent 2e$^-$ ORR performance for H_2O_2 production, achieving a selectivity of 97% and a robust ring current across a broad potential window from 0.1 to 0.7 V *vs.* RHE in alkaline media. Our calculated results further illustrated that the high performance of the Pd@$Pd_{SA}N_{2\text{-}2}C$ catalyst for 2e$^-$ ORR can be again attributed to the centrosymmetric PdN_4 structure in the shell, which maintains a structure similar to $Pd_{SA}N_{2\text{-}2}C$, as well as the existence of Pd core that can modulate the *d*-orbital arrangement of the single Pd atom in the shell. Within a gas diffusion electrode integrated flow-cell setup, Pd@$Pd_{SA}N_{2\text{-}2}C$ achieved a high H_2O_2 yield of 35.88 mol g_{cat}^{-1} h^{-1} at 200 mA cm^{-2} with over 80% selectivity, alongside a cumulative H_2O_2 concentration of 34.27 g L^{-1} over 1080 min, surpassing previously reported metal single-atom electrocatalysts. This work not only provides a deeper understanding of the structural and electronic features of the M-N-C materials in electrocatalytic reactions, it also offers valuable guidance for the development of highly efficient electrocatalysts for H_2O_2 production.

Author contributions

The manuscript was written through contributions of all authors. All authors have given approval to the final version of the manuscript. ‡These authors contributed equally.

Conflicts of interest

The authors declare no competing financial interest.

Data availability

Data related to ORR mechanism, computational details, chemicals and reagents, physicochemical characterizations and electrochemical tests are provided in Supplementary Information.

Acknowledgements

This work was supported by the National Key R&D Program of China (2024YFA1509901, 2023YFA1508500, 2021YFA1500700) and the National Nature Science Foundation of China (22572049, 22203030).

References

1 H. Liu, L. Jiang, Y. Sun, J. Khan, B. Feng, J. Xiao, H. Zhang, H. Xie, L. Li, S. Wang, L. Han, *Adv. Energy Mater*, 2023, **13**, 2301223.
2 B. Yue, L. Lei, H. Xie, Y. Si, Q. Yang, X. Liu, *ACS Appl. Mater. Interfaces*, 2023, **15**, 33665-33674.
3 Q. Zhang, X. Tan, N. M. Bedford, Z. Han, L. Thomsen, S. Smith, R. Amal, X. Lu, *Nat. Commun.*, 2020, **11**, 4181.
4 D. Zhang, F. She, J. Chen, L. Wei, H. Li, *J. Am. Chem. Soc.*, 2025, **147**, 6076-6086.
5 H. T. Chung, D. A. Culle, D. Higgins, B. T. Snee, E. F. Holb, K. L. More, P. Zelenay, *Science*, 2017, **357**, 479-484.
6 K. Kumar, L. Dubau, F. Jaouen, F. Maillard, *Chem. Rev.*, 2023, **123**, 9265-9326.
7 L. Yan, P. Li, Q. Zhu, A. Kumar, K. Sun, S. Tian, X. Sun, *Chem.*, 2023, **9**, 280-342.
8 H. Huang, M. Sun, S. Li, S. Zhang, Y. Lee, Z. Li, J. Fang, C. Chen, Y.-X. Zhang, Y. Wu, Y. Che, S. Qian, W. Zhu, C. Tang, Z. Zhuang, L. Zhang, Z. Niu, *J. Am. Chem. Soc.*, 2024, **146**, 9434-9443.
9 Z. Levell, S. Yu, R. Wang, Y. Liu, *J. Am. Chem. Soc.*, 2025, **147**, 603-609.
10 Y. Wang, R. Shi, L. Shang, G. I. N. Waterhouse, J. Zhao, Q. Zhang, L. Gu, T. Zhang, *Angew. Chem. Int. Ed.*, 2020, **59**, 13057-13062.
11 J. Gao, B. Liu, *ACS Mater. Lett.*, 2020, **2**, 1008-1024.
12 S. Chen, T. Luo, X. Li, K. Chen, J. Fu, K. Liu, C. Cai, Q. Wang, H. Li, Y. Chen, C. Ma, L. Zhu, Y.-R. Lu, T.-S. Chan, M. Zhu, E. Cortés, M. Liu, *J. Am. Chem. Soc.*, 2022, **144**, 14505-14516.
13 W. Wang, Y. Hu, P. Li, Y. Liu, S. Chen, *ACS Catal.*, 2024, **14**, 5961-5971.
14 N. Zhang, T. Zhou, M. Chen, H. Feng, R. Yuan, C. Zhong, W. Yan, Y. Tian, X. Wu, W. Chu, C. Wu, Y. Xie, *Energy Environ. Sci.*, 2020, **13**, 111-118.
15 B. Ni, P. Shen, G. Zhang, J. Zhao, H. Ding, Y. Ye, Z. Yue, H. Yang, H. Wei, K. Jiang, *J. Am. Chem. Soc.*, 2024, **146**, 11181-11192.
16 H. Xu, D. Cheng, D. Cao, X. C. Zeng, *Nat. Catal.*, 2024, **7**, 207-218.
17 J. Gao, H. Yang, X. Huang, S.-F. Hung, W. Cai, C. Jia, S. Miao, H. M. Chen, X. Yang, Y. Huang, T. Zhang, B. Liu, *Chem.*, 2020, **6**, 658-674.
18 K. Jiang, S. Back, A. J. Akey, C. Xia, Y. Hu, W. Liang, D. Schaak, E. Stavitski, J. K. Nørskov, S. Siahrostami, H. Wang, *Nat. Commun.*, 2019, **10**, 3997.
19 N. Wang, X. Zhao, R. Zhang, S. Yu, Z. H. Levell, C. Wang, S. Ma, P. Zou, L. Han, J. Qin, L. Ma, Y. Liu, H. L. Xin, *ACS Catal.*, 2022, **12**, 4156-4164.
20 Y. L. Wang, S. Gurses, N. Felvey, A. Boubnov, S. S. Mao, C. X. Kronawitter, *ACS Catal.*, 2019, **9**, 8453-8463.
21 Z. Wei, B. Deng, P. Chen, T. Zhao, S. Zhao, *Chem. Eng. J.*, 2022, **428**, 131112.
22 T. Zhang, W. Wang, W. Liu, Z. Guo, J. Liu, *Nat. Commun.*, 2025, **16**, 5240.
23 T. Wu, M. Sun, B. Huang, *Mater. Today Energy*, 2019, **12**, 426e430.
24 J. S. Spendelow, A. Wieckowski, *Phys. Chem. Chem. Phys.*, 2007, **9**, 26542675.
25 S. C. Perry, D. Pangotra, L. Vieira, L.-I. Csepei, V. Sieber, L. Wang, C. P. León, F. C. Walsh, *Nat. Rev. Chem.*, 2019, **3**, 442-458.
26 B. Xia, Q. Huang, K. Wu, L. Jiang, M. Li, L. Yu, S. Ding, Z. Nie, D. Hua, J. Duan, S. Chen, *AIChE J.*, 2023, **69**, e18022.
27 R. Shen, R. Shen, W. Chen, Q. Peng, S. Lu, L. Zheng, X. Cao, Y. Wang, W. Zhu, J. Zhang, Z. Zhuang, C. Chen, D. Wang, Y. Li, *Chem.*, 2019, **5**, 2099-2110.
28 Y. Sun, L. Silvioli, N. R. Sahraie, W. Ju, J. Li, A. Zitolo, S. Li, A. Bagger, L. Arnarson, X. Wang, T. Moeller, D. Bernsmeier, J. Rossmeisl, F. Jaouen, P. Strasser, *J. Am. Chem. Soc.*, 2019, **141**, 12372-12381.
29 J. Du, S. Jiang, R. Zhang, P. Wang, C. Ma, R. Zhao, C. Cui, Y. Zhang, Y. Kang, *ACS Catal.*, 2023, **13**, 6887-6892.
30 S. Zhang, Z. Tao, M. Xu, L. Kan, C. Guo, J. Liu, L. He, M. Du, Z. Zhang, *Small*, 2024, **20**, 2310468.
31 Q. Chang, P. Zhang, A. H. B. Mostaghimi, X. Zhao, S. R. Denny, J. H. Lee, H. Gao, Y. Zhang, H. L. Xin, S. Siahrostami, J. G. Chen, Z. Chen, *Nat. Commun.*, 2020, **11**, 2178.
32 G. Kresse, J. Furthmüller, *Phys. Rev. B*, 1996, **54**, 11169.
33 G. Kresse J., Hafner, *Phys. Rev. B*, 1993, **47**, 558.
34 G. Kresse, J. Hafner, *Phys. Rev. B*, 1994, **49**,14251.
35 G. Kresse, J. Furthmüller, *Comput. Mater. Sci.*, 1996, **6**, 15-50.

View Article Online
DOI: 10.1039/D5SC09543C

36 J. P. Perdew, J. A. Chevary, S. H. Vosko, K. A. Jackson, M. R. Pederson, D. J. Singh, C. Fiolhais, *Phys. Rev. B*, 1992, **46**, 6671.
37 M. P. Teter, M. C. Payne, D. C. Allan, *Phys. Rev. B*, 1989, **40**, 12255-12263.
38 P. E. Blöchl, *Phys. Rev. B*, 1994, **50**, 17953.
39 G. Kresse, D. Joubert, *Phys. Rev. B*, 1999, **59**, 1758-1775.
40 Z. Su, H. Wei, L. Zhang, H. Li, P. Liu, Z. Hou, X. Gong, *Electrochim. Acta*, 2023, **468**, 143180.
41 Y. Yuan, J. Ma, B. Kang, J. Y. Lee, *ACS Catal.*, 2025, **15**, 4039-4050.
42 C. Tang, L. Chen, H. Li, L. Li, Y. Jiao, Y. Zheng, H. Xu, K. Davey, S.-Z. Qiao, *J. Am. Chem. Soc.*, 2021, **143**, 7819-7827.
43 E. Jung, H. Shin, B.-H. Lee, V. Efremov, S. Lee, H. S. Lee, J. Kim, W. H. Antink, S. Park, K.-S. Lee, S.-P. Cho, J. S. Yoo, Y.-E. Sung, T. Hyeon, *Nat. Mater.*, 2020, **19**, 436-442.
44 X. Guo, S. Lin, J. Gu, S. Zhang, Z. Chen, S. Huang, *ACS Catal.*, 2019, **9**, 11042-11054.
45 Y. Zou, X. Guo, X. Bian, Y. Zhang, W. Lin, S. Huang, Z. Chen, K. Ding, *Appl. Surf. Sci.*, 2022, **592**, 153233.
46 X. Chen, H. Zhu, J. Zhu, H. Zhang, *Chem. Eng. J.*, 2023, **451**, 138998.
47 Q. Liu, X. Bian, S. Xie, W. Ruan, W. Chen, X. Guo, K. Ding, *Int. J. Hydrogen Energ.*, 2024, **51**, 1413-1420.
48 Q. Wu, H. Zou, X. Mao, J. He, Y. Shi, S. Chen, X. Yan, L. Wu, C. Lang, B. Zhang, L. Song, X. Wang, A. Du, Q. Li, Y. Jia, J. Chen, X. Yao, *Nat. Commun.*, 2023, **14**, 6275.
49 H. Gong, L. Wei, S. Chen, Z. Chen, T. F. Jaramillo, Z. Bao, *Nano Res.*, 2023, **16**, 11556-11563.
50 J. Su, L. Jiang, B. Xiao, Z. Liu, H. Wang, Y. Zhu, J. Wang, X. Zhu, *Small*, 2024, **20**, 2310317.
51 S. Wei, A. Li, J.-C. Liu, Z. Li, W. Chen, Y. Gong, Q. Zhang, W.-C. Cheong, Y. Wang, L. Zheng, H. Xiao, C. Chen, D. Wang, Q. Peng, L. Gu, X. Han, J. Li, Y. Li, *Nat. Nanotech.*, 2018, **13**, 856-861.

View Article Online
DOI: 10.1039/D5SC09543C

Data related to ORR mechanism, computational details, chemicals and reagents, physicochemical characterizations and electrochemical tests are provided in Supplementary Information.